NANO LETTERS
Letter
pubs.acs.org/NanoLett

Spatially Mapping Energy Transfer from Single Plasmonic Particles to Semiconductor Substrates via STEM/EELS

Guoliang Li,[†] Charles Cherqui,[‡] Nicholas W. Bigelow,[‡] Gerd Duscher,[§] Patrick J. Straney,[∥]
Jill E. Millstone,[∥] David J. Masiello,*[,‡] and Jon P. Camden*[,†]

[†]Department of Chemistry and Biochemistry, University of Notre Dame, Notre Dame, Indiana 46556, United States
[‡]Department of Chemistry, University of Washington, Seattle,Washington 98195, United States
[§]Department of Materials Science and Engineering, University of Tennessee, Knoxville, Tennessee 37996, United States
[∥]Department of Chemistry, University of Pittsburgh, Pittsburgh, Pennsylvania 15260, United States

Supporting Information

ABSTRACT: Energy transfer from plasmonic nanoparticles to semiconductors can expand the available spectrum of solar energy-harvesting devices. Here, we spatially and spectrally resolve the interaction between single Ag nanocubes with insulating and semiconducting substrates using electron energy-loss spectroscopy, electrodynamics simulations, and extended plasmon hybridization theory. Our results illustrate a new way to characterize plasmon−semiconductor energy transfer at the nanoscale and bear impact upon the design of next-generation solar energy-harvesting devices.

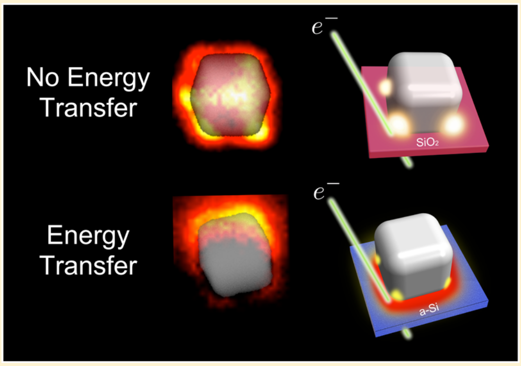

KEYWORDS: *STEM, EELS, energy transfer, plasmonics, photovoltaics, nanocubes*

Localized surface plasmon resonances (LSPRs), the collective and coherent optical-frequency excitations of a metal nanoparticle's conduction band electrons, can localize light below the diffraction limit and generate intense electric near-fields.[1] This unique property has been exploited in applications ranging from single-molecule spectroscopy[2] to molecular sensing[3] and photothermal cancer therapy.[4] Beyond these applications, plasmonically active nanoparticles have been incorporated in the design of photovoltaic (PV) and photocatalytic devices, where they have been shown to enhance solar energy-harvesting efficiency.[5−21] The rate-limiting step of any semiconductor-based PV device is the conversion of solar energy into electron−hole pairs, which in a traditional solar cell is dictated by the direct interaction of light with the semiconductor. The addition of plasmonic nanoparticles adds an intermediary between the light and semiconductor, thereby opening new energy-harvesting pathways.

The interaction of metal nanoparticles with a dielectric substrate serves as a model for understanding the flow of plasmonic energy in solar devices. Experiments on related systems have shown that the addition of plasmonic nanoparticles improves the efficiency of solar light-harvesting via one or more of the following mechanisms: (1) the LSPR excitation leads to an increase in path length for incoming light via scattering, thereby increasing the probability of photon absorption by the substrate;[10−12] (2) energy transfer from the decay of an LSPR directly creates an electron−hole pair in the neighboring semiconductor, a process known as plasmon-induced resonant energy transfer (PIRET);[13−16] or (3) direct electron transfer (DET) from the nanoparticle to the substrate,[14−17,21−27] in which an LSPR decays, through Landau damping,[25,28] into an energetic electron (a so-called "hot" electron) that may then scatter into the semiconductor if it has sufficient energy. Though hot electrons carry energy away from the metal, it is not solely an energy transfer mechanism since it includes electron transport from the metal to the neighboring semiconductor and therefore leads to a change in the number of charge carriers. However, for the purpose of the work presented here, this distinction is of no consequence, and we refer to both as energy transfer pathways. Both PIRET and DET stem from the LSPR−substrate coupling and constitute light-harvesting mechanisms absent in nonplasmonic PV devices. These mechanisms can be further divided into radiative and nonradiative contributions; mechanism 1 involves the absorption of solar radiation by the semiconductor and is only effective for photon energies above the semiconductor band gap, while mechanisms 2 and 3 involve solar photons with energies below or above the band gap.[14,15] Mechanisms 2 and 3 are of particular interest and importance as they expand the

Received: February 27, 2015
Revised: April 2, 2015

© XXXX American Chemical Society

DOI: 10.1021/acs.nanolett.5b00802

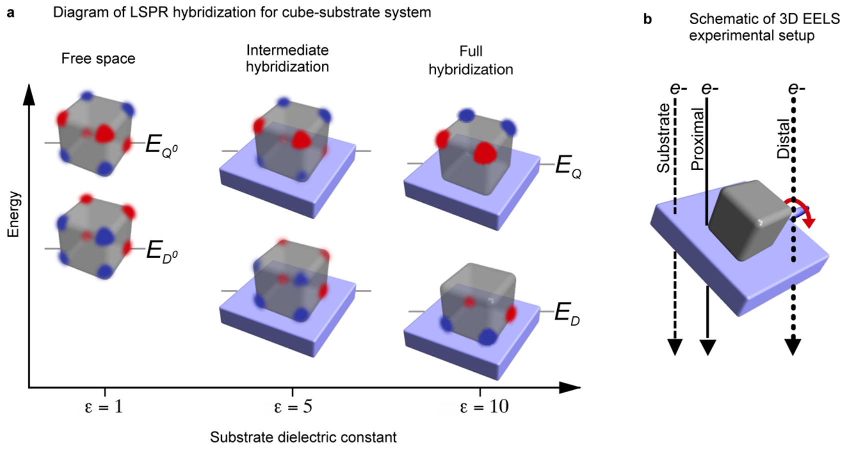
a
Diagram of LSPR hybridization for cube-substrate system
Free space
Intermediate hybridization
Full hybridization
Energy
E_{Q^0}
E_{D^0}
E_Q
E_D
ε = 1
ε = 5
ε = 10
Substrate dielectric constant
b
Schematic of 3D EELS experimental setup
e-
e-
e-
Substrate
Proximal
Distal

Figure 1. Correlation diagram of substrate-induced LSPR hybridization in the cube@substrate system and EELS experimental setup. (a) Diagram of substrate-induced LSPR hybridization of a Ag nanocube. The evolution of the surface charge distributions of the D and Q eigenmodes of the nanocube is schematically displayed as a function of increasing substrate dielectric constant. (b) Experimental EELS setup. The electron beam independently addresses the proximal and distal corners of the nanocube by tilting the composite system. The substrate is probed at a beam position far from the nanocube.

solar spectrum available for energy conversion. However, despite its importance, little is known about how energy transfer operates at the nanoscale, particularly at the level of a single nanoparticle and its supporting substrate.

The Ag nanocube on a dielectric substrate[29−35] is a model system for the study of energy transfer in single nanoparticle–semiconductor systems, as both theory and experiment demonstrate that the LSPR mode structure of cubes is highly sensitive to changes in the dielectric environment.[34] The free-space LSPR modes of a Ag nanocube concentrate surface charge on the cube corners (corner modes), edges (edge modes), and faces (face modes).[33] In vacuum, the lowest energy plasmon eigenmodes of the nanocube are the corner dipole (D^0) and corner quadrupole (Q^0) modes (Figure 1a). In the presence of a substrate the reduced symmetry allows the mixing of D^0 and Q^0 through the image response of the substrate, resulting in new hybridized modes D and Q. These renormalized modes are linear combinations of the free-space modes and range in character from D^0 and Q^0 dominated to surface charge distributions that are fully substrate- or vacuum-localized (Figure 1a). This localization effect, which is closely related to the plasmonic Fano interference effect, has been the focus of an intense research effort in recent years.[34−42] As the dielectric constant of the substrate is increased, D exhibits stronger substrate localization while Q exhibits stronger vacuum localization.[34]

The substrate-localized D mode, which confines the surface charge to the cube@substrate interface, is an ideal candidate for the study of energy transfer. For PIRET, the substrate-localized D mode provides the strongest possible coupling between the LSPR and the induced electronic dipole moment of the semiconductor. For DET, the D mode ensures the close proximity of any hot electrons born from the decay of an LSPR to the cube@substrate interface. In contrast, the vacuum-localized Q mode does not strongly interact with the substrate as the surface charge for this mode is localized far from the substrate, allowing us to focus only on the behavior of the D mode.

If plasmonic nanoparticles are going to be efficiently implemented in PV designs,[23] the ability to characterize the near-field signature of energy transfer must be refined. In this paper, we present the first nanoscopic view of energy flow between single, well-characterized Ag nanocubes and their underlying substrates via electron energy-loss spectroscopy (EELS) performed in a scanning transmission electron microscope (STEM). In particular, we provide a method for obtaining the spatial profile of energy transfer on the nanocube. As PIRET and DET can occur simultaneously, we vary the optical and electronic properties of the substrate to isolate these respective energy transfer mechanisms. This is accomplished by synthesizing nanocubes with nearly identical dimensions and repeating the experiment on three different substrates: one insulating substrate, silicon dioxide (SiO_2), and two semiconducting substrates, crystalline boron phosphide (BP) and amorphous silicon (a-Si).[43] When the experimental observations are taken together with an extended plasmon hybridization model[44,45] (Supporting Information) and full-wave EELS simulations via the electron-driven discrete dipole approximation (e-DDA),[46,47] the spatial and spectral signatures of energy transfer are revealed. Previous experimental studies of plasmonic energy transfer have commonly relied on optical spectroscopy[16,22,48] using far-field light and are restricted by the diffraction limit. In contrast, the high degree of spatial and energy resolution provided by STEM/EELS allows us to observe energy transfer at the nanoscale. This work provides the first near-field characterization of energy transfer on well-characterized nanoparticle systems and expands our basic understanding of the LSPR–semiconductor interaction, facilitating the design of future high-efficiency plasmon-enhanced solar energy-harvesting devices.

The experimental setup is described schematically in Figure 1b. EELS experiments are carried out in a monochromated Carl Zeiss LIBRA 200MC (S)TEM operated at 200 kV. A region of interest (ROI) consisting of 900 pixels (1 pixel ∼ 4 nm × 4 nm) is defined over the tilted cube@substrate system, and EEL spectra are acquired pixel by pixel while the focused electron probe is rastered over the ROI. Tilting the cube@substrate system allows us to *selectively* excite the corner D mode, reducing the contribution from admixtures with edge and face modes.[33] Selective excitation is possible because the D mode is the lowest energy mode and is well separated from the higher energy modes. As long as the tilting angle accomplishes isolation of the D mode, it has no further impact on the experiment. Difficulties related to finding cube@substrate systems with similar substrate thickness, cube size, and low contamination levels make tilting each system to the same angle impractical.

To explore a variety of optical and electronic properties, we utilize both commercial and in-house fabricated TEM membranes. The employed substrates and their selected properties are listed in Table 1.[49−58] The SiO_2 membrane is a commercial product widely used for TEM. BP and a-Si membranes are fabricated via conventional TEM specimen preparation procedures.[59] The edge lengths of the studied Ag nanocubes range from 71 to 77 nm. Details about substrate preparation, characterization, and planview TEM images of the studied cubes can be found in the Supporting Information.

Table 1. Selected Properties of Employed Substrates[49−58]

substrate	$\varepsilon_1{}^a$	$\varepsilon_2{}^a$	$E_g{}^b$ (eV)	$E_{opt}{}^c$ (eV)	t^d (nm)
SiO_2	2.3	0	9.0	10.6	30
BP	9.6	0	2.1	4.3	38
a-Si	17.5	3.4	1.7	1.7	26

[a] ε_1 and ε_2 are the real and imaginary parts of the dielectric constant at 633 nm, respectively. [b] E_g is the band gap of the substrate material. [c] E_{opt} is the optical or the lowest direct band gap of the substrate material. [d] t is the calculated substate thickness (Supporting Information).

The EEL spectra, Z-contrast images, and EEL probability maps of the cube@SiO_2/BP/a-Si systems are shown in Figure 2. Figure 2a displays EEL spectra acquired at the proximal and distal corners of the cube. The EEL spectra acquired far from the cube are also included to show the background signal due to the substrate. Figure 2b is a collection of Z-contrast images of the tilted cube@SiO_2/BP/a-Si systems, in which the background color is tuned from black to red, green, and blue, respectively, to increase the visibility of the cube edges. Figures 2c,d show the EEL probability map at the resonance energies of D and Q (E_D and E_Q) over the spatial ROI, showing the spatial distribution of the EEL probability.

The EEL probability maps (Figure 2c,d) for the cube@SiO_2 system are in agreement with previous studies of cube@insulator systems,[29−34] showing substrate- and vacuum-localization for the D and Q mode, respectively. Interestingly, both D-mode maps (Figure 2c) for the cube@BP and cube@a-Si systems exhibit almost zero EEL probability near the proximal corners, in sharp contrast to the substrate localization seen in the cube@SiO_2 system. As will be demonstrated in the following, we interpret the low EEL probability of the D mode at the proximal corners in the cube@BP and cube@a-Si systems as a near-field signature of energy transfer.

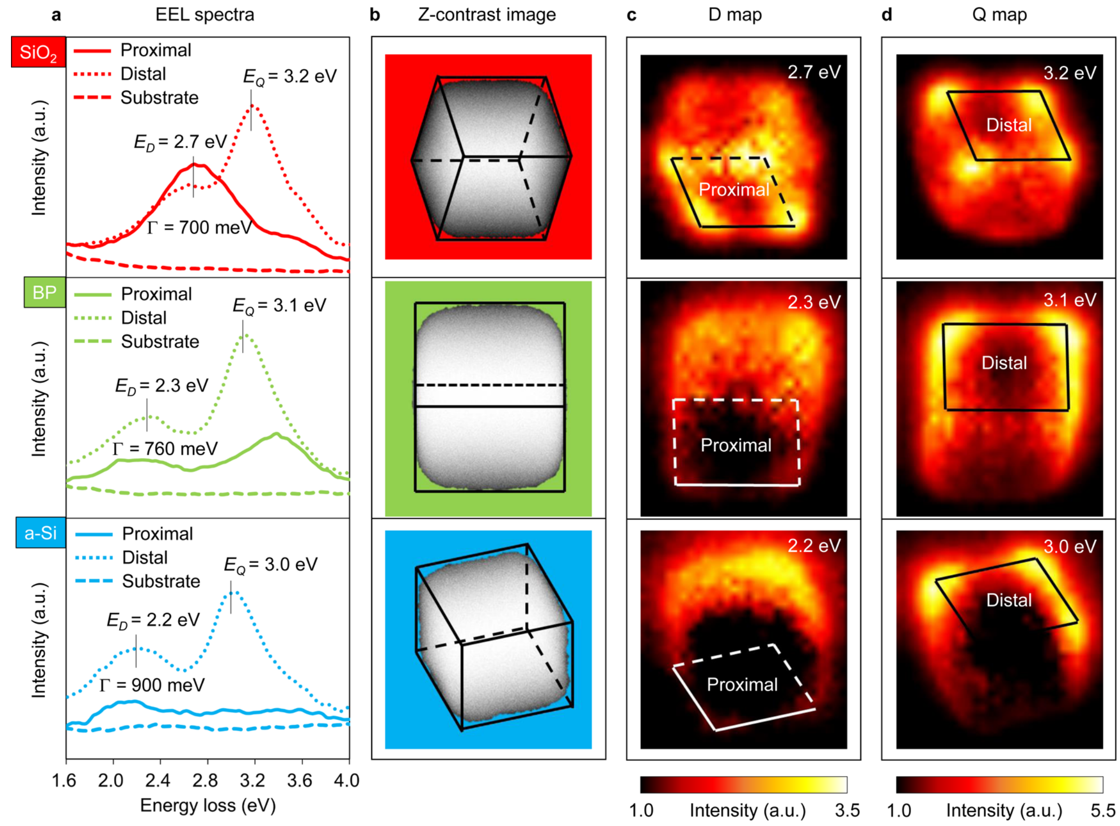

Figure 2. EEL spectra, Z-contrast images, and EEL probability maps. (a) EEL spectra acquired at the proximal (solid lines) and distal (dotted lines) corners of the cube, and substrate (dashed lines), as described in Figure 1b. These spectra are normalized by corresponding zero-loss intensities. The impact parameter for the proximal and distal EEL spectra is approximately 1 pixel (4 nm) from the cube surface in all cases. The substrate EEL spectra are acquired at a beam position far from the cube. E_D and E_Q denote the resonant energies, while Γ denotes the line width of the D mode. (b) Z-contrast images of the tilted cubes. The solid lines represent the cube edges that are visible when viewed into the page, whereas the dashed lines represent cube edges that are blocked in the viewing direction. (c, d) Experimental D- and Q-mode EEL probability maps generated by plotting the spectral intensity over the ROI at E_D (c) and E_Q (d). The proximal and distal faces are shown in the maps. *The near-zero EEL probability in the D-mode map at the cube@BP and cube@a-Si interfaces is a signature of energy transfer to the substrate.*

DOI: 10.1021/acs.nanolett.5b00802

As was mentioned above, only the substrate-localized D mode significantly contributes to energy transfer, making the Q mode irrelevant to the subsequent discussion. However, as can be seen in Figure 2a, the Q mode is a prominent feature in the distal EEL spectra. For this reason, we include the Q-mode maps to show consistency between our work and previous studies.[31−34] To gain a metric for energy transfer, we fit the lowest energy peak in each distal EEL spectra to obtain an empirical measure of the D-mode line width, Γ (Figure 2a).

We begin by exploring theoretically the signature of PIRET in the D-mode map (Figure 2c). PIRET arises from the near-field coupling between a metal nanoparticle LSPR and an adjacent semiconductor and is similar to the well-studied Förster resonant energy transfer (FRET) mechanism.[14,16] The plasmonic dipole moment induces a transition dipole moment in the nearby semiconductor, which, through induced dipole−dipole coupling, results in the decay of an LSPR into a bound electron−hole pair in the substrate.[13−16]

To understand how the EEL probability map and EEL spectra of the D mode is affected by PIRET, we now construct two different theoretical models. First, we calculate the D-mode map and EEL spectra of a model cube@substrate system using e-DDA simulations. The optical response of the cube is parametrized by experimental dielectric data for Ag,[60] while the substrate is characterized by a Lorentz oscillator dielectric function $\varepsilon(\omega;E_{\mathrm{opt}}/\hbar)$, with an optical band gap energy of E_{opt} and a driving frequency of ω. This model allows us to selectively turn the PIRET pathway on and off by changing the value of E_{opt}. To model a semiconductor (PIRET on), we set $E_{\mathrm{opt}} \simeq E_{\mathrm{D}}$, and to model an insulator (PIRET off), we set $E_{\mathrm{opt}} \gg E_{\mathrm{D}}$. The resulting D-mode maps for both systems are shown in Figure 3a. In the cube@insulator map, we find high EEL probability at the proximal corners of the cube, consistent with the cube@SiO$_2$ D-mode map (Figure 2c). In the cube@semiconductor map, we observe a significant reduction of EEL probability near the substrate, indicating energy transfer. This is in contrast to the cube@insulator map, but in qualitative agreement with the cube@BP/a-Si D-mode maps (Figure 2c). The difference in intensity in the D-mode maps for the model system shows that in the case of PIRET the EEL probability map is correlated with the spatial profile of energy transfer. In addition to this decrease in intensity, we also see an increase in line width in the corresponding EEL spectra (Figure 3b), suggesting that line width broadening is also associated with energy transfer.

Second, we develop an extended plasmon hybridization model[44,45] (Supporting Information) to describe the above-mentioned cube@semiconductor system, giving an analytical understanding of how the D-mode line width is related to PIRET. Within this model, we keep E_{opt} constant and treat $\hbar\omega = E_{\mathrm{D}}$ as a free parameter. This allows us to estimate the overall amount of line width broadening due to PIRET. The LSPR dipole moment is modeled as a damped harmonic oscillator being driven self-consistently by the image response of the substrate. The substrate-dressed damping coefficient of the LSPR oscillator is equal to the hybridized D-mode line width Γ_{H}, which, in the limit of full hybridization (Figure 1a), takes the form

$$\Gamma_{\mathrm{H}} \simeq \Gamma_{\mathrm{I}}\left\{1 + \mathrm{Im}\left[\frac{\varepsilon(\omega;\, E_{\mathrm{opt}}/\hbar) - 1}{\varepsilon(\omega;\, E_{\mathrm{opt}}/\hbar) + 1}\right]\frac{Q\alpha_{\mathrm{sp}}}{(2d)^3}\right\} \qquad (1)$$

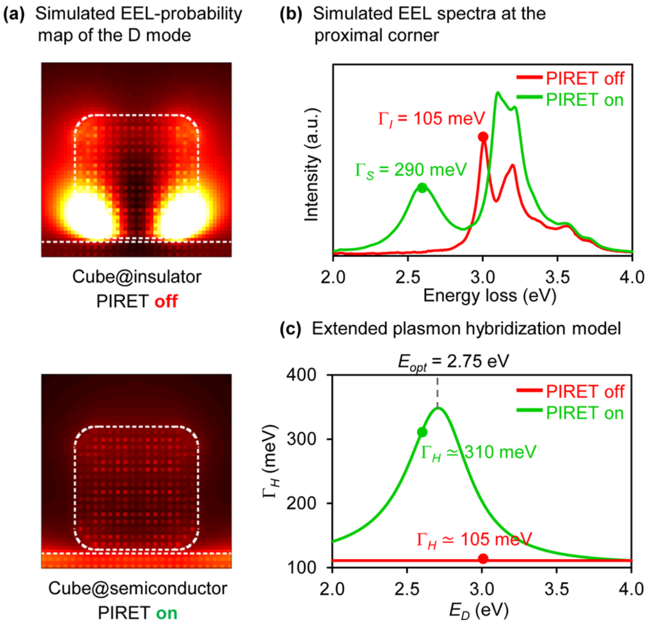

Figure 3. Theoretical study of the effect of PIRET on D-mode map, EEL spectra, and line width. (a) Simulated D-mode EEL probability map for the cube@insulator (PIRET off, upper panel) and cube@semiconductor (PIRET on, lower panel) model systems. The cube@insulator system ($E_{\mathrm{opt}} \gg E_{\mathrm{D}}$) shows highest EEL probability at the proximal corners of the cube (substrate localization). The cube@semiconductor system (E_{opt} = 2.75 eV) shows a sharp reduction in EEL probability at the proximal corners, a signature of energy transfer and consistent with the experimental observations. The white lines are outlines of the cube and the substrate. (b) Simulated EEL spectra for cube@insulator and cube@semiconductor systems for a proximal beam position. The difference in line width between the PIRET off (red curve) and PIRET on (green curve) spectra is due to energy transfer. The D-mode line width for the cube@semicondictor system (Γ_{S} = 290 meV) is approximately 3 times greater than the cube@insulator D-mode line width (Γ_{I} = 105 meV); this effect is accompanied by a drop in EEL probability intensity. (c) Extended plasmon hybridization model of the D-mode line width (Γ_{H}) is plotted as a function of E_{D} for PIRET off (red curve) and PIRET on (green curve). At $E_{\mathrm{opt}} \simeq E_{\mathrm{D}}$, the PIRET on system exhibits the maximum amount of line width broadening due to PIRET. The line width predicted by the hybridization model is in good agreement with the simulation results shown in (b); the green and red dots correspond to the simulated D-mode energies for PIRET on and PIRET off, respectively.

Here, Q is the quality factor of the cube@insulator D mode, α_{sp} is the static polarizability of the cube, d is the distance between the LSPR and its image in the substrate, and Γ_{I} is the cube@insulator D-mode line width discussed above (PIRET off), which serves as a baseline to estimate PIRET-induced line width broadening. Equation 1 is plotted in Figure 3c as a function of E_{D} and has a resonance when $E_{\mathrm{D}} \simeq E_{\mathrm{opt}}$. This resonance corresponds to a maximum amount of line width broadening due to PIRET and therefore a maximum amount of energy transfer from the cube to the semiconductor. As is shown in Figure 3c, the amount of PIRET-induced line width broadening predicted in the analytical model is in good agreement with the e-DDA simulations of the model cube@substrate system described above (Figure 3b). The conclusions drawn from both approaches are that the intensity reduction in the D-mode map at the proximal corners of the cube and the associated line width broadening in the EEL spectrum are

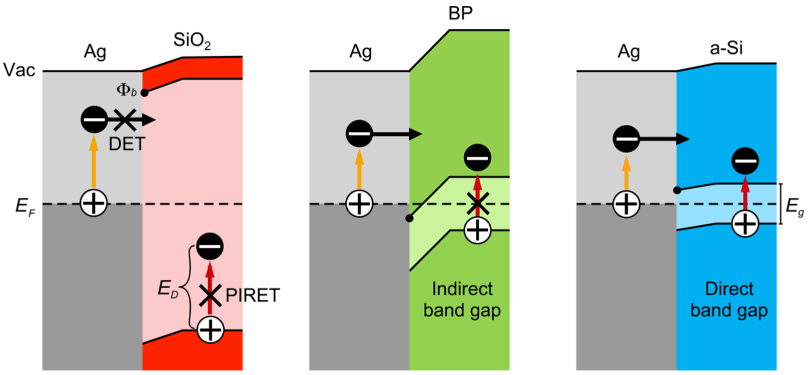

Figure 4. Band diagrams and available energy transfer pathways for cube@SiO_2/BP/a-Si systems. The cube@SiO_2 system (left) has both DET and PIRET channels closed due to the insulating properties of SiO_2. Φ_b is the Schottky barrier and denoted by a black dot in each system. The cube@BP system (center) has DET open (Δ = +2.9 eV) but PIRET closed because of the negligible absorbance of BP in the optical range. The cube@a-Si system (right) has both DET (Δ = +1.7 eV) and PIRET channels open.

signatures of PIRET. Though neither the classical e-DDA simulations nor the analytical model take the quantum-mechanical DET mechanism into account, it is known to lead to a similar line width broadening.[22]

In the DET process, hot electrons are generated through the Landau damping of LSPRs,[25] with a resulting electron energy distribution centered about the resonance energy of the plasmon.[61] These nascent hot electrons may then scatter into the conduction band of the nearby semiconductor if they have sufficient energy to overcome the Schottky barrier (Φ_b).[23] The difference in energy between the LSPR and the Schottky barrier (Φ_b) determines whether or not DET can occur,[7−9,18] and the "hotter" an electron is with respect to Φ_b, the higher the probability that it will scatter into the semiconductor. For the cube@substrate systems considered here, it is the decay of the D mode that provides the flux of hot electrons, and the energy difference $\Delta = E_D - \Phi_b$ determines the likelihood of DET. We assume DET to be an open channel if Δ is positive.

We summarize the available energy transfer pathways for all three cube@substrate systems in Figure 4. The cube@SiO_2 system is not expected to exhibit energy transfer since it is an optically transparent large band gap insulator ($E_{opt} \gg E_D$, $\Delta = -0.7$ eV). The cube@BP system is particularly interesting as BP is transparent at optical frequencies ($E_{opt} > E_D$); i.e., it has a static dielectric response, leaving DET as the only open energy transfer pathway. Furthermore, Δ_{BP} = +2.9 eV suggests that DET will be an efficient channel. The cube@a-Si system has both energy transfer pathways open as a-Si has a small optical band gap ($E_{opt} < E_D$) and a value of $\Delta_{a\text{-}Si}$ = +1.7 eV.

With the theoretical descriptions of energy transfer in mind, we return to the analysis of the data. As expected, the cube@SiO_2 system shows a clearly substrate-localized D mode (Figure 2c). The lack of energy transfer in the cube@SiO_2 system provides a baseline from which to compare other configurations. The energy transfer supporting systems, cube@BP and cube@a-Si, show highly damped D-mode maps with near-zero EEL-probability at the proximal corners of the cubes. This is a signature of energy transfer and allows us to determine where the energy transfer occurs with nanoscale spatial resolution. To our knowledge, this is the first report of the STEM/EELS spatial mapping of energy transfer in coupled LSPR−semiconductor systems.

To further interpret these observations, we compute the EEL spectra using e-DDA for both the cube@BP and cube@a-Si systems (Supporting Information Figure 5) and obtain the simulated values of Γ = 330 meV for BP and Γ = 410 meV for a-Si. The dielectric data for both Ag[60] and substrate materials[56−58] are taken from experiments. The simulation results are less than half the value obtained from experiment (Γ = 760 meV for BP, Γ = 900 meV for a-Si). Since the PIRET pathway is accounted for in the classical e-DDA simulations, we attribute the large difference in line width between theory and experiment to DET. This suggests that the DET channel plays a dominant role in both systems, even though the cube@a-Si system has both channels open. This conclusion is supported by the *excellent agreement* between the full wave e-DDA simulations and the experimental EELS data in the cube@SiO_2 system, where all energy transfer channels are closed (compare Γ = 700 meV from experiment to Γ = 670 meV from simulation). The results for BP suggest that optically transparent materials could be used to fabricate PV devices that rely solely on plasmonic energy transfer via DET, in contrast to the usual electron−hole pair generation mechanism found in traditional devices.

The approach presented here can be extended in many directions beyond solar devices. For example, the semiconductor can be replaced with redox-active molecules, harvesting the hot electrons produced by the nanoparticle to drive plasmon-assisted catalysis. The localization of the D and Q modes could be exploited to act as an energy transfer switch by tuning the excitation energy, for example, in a semiconductor/cube/semiconductor interface. The nanocube shares a flat surface with the adjacent semiconductor and other geometries such as disks, truncated spheres, or pyramids should be explored to further understand the role of contact area in DET. In this same vein, this work can be extended to investigate the dependence of LSPRs on nanoparticle geometry to determine the role of morphology in energy transfer, a task to which EELS is well suited. Additionally, the dependence of energy transfer pathways on the surface electronic structure of doped semiconductors can be optimized.

In conclusion, we have demonstrated the ability of STEM/EELS experiments to elucidate the nanoscopic flow of energy from a light-harvesting plasmonic nanostructure into its semiconducting substrate. We correlated our experiments with full-wave electrodynamics simulations and extended plasmon hybridization theory to demonstrate that the EEL probability map can provide a spatial profile of energy transfer at the single-particle level. The work presented here provides researchers with new methods to probe competing energy

DOI: 10.1021/acs.nanolett.5b00802

transfer mechanisms in hybrid nanoparticle@semiconductor systems. The fundamental understanding of plasmonic energy transfer that we provide will help improve the efficiency of future PV and photocatalytic devices.

■ ASSOCIATED CONTENT

Ⓢ Supporting Information

Information on (i) Ag nanocube synthesis, (ii) TEM substrate preparation and characterization, (iii) EELS experiments and EEL probability map generation, (iv) e-DDA simulations, and (v) extended plasmon hybridization model. This material is available free of charge via the Internet at http://pubs.acs.org.

■ AUTHOR INFORMATION

Corresponding Authors

*E-mail jon.camden@nd.edu (J.P.C.).
*E-mail masiello@chem.washington.edu (D.J.M.).

Author Contributions

G.L. and C.C. contributed equally to this work.

Notes

The authors declare no competing financial interest.

■ ACKNOWLEDGMENTS

C.C. thanks Niket Thakkar and G.L. thanks Ondrej E. Dyck for helpful discussions. This work was supported by the U.S. National Science Foundation's CAREER program under Award CHE-1253775 and through XSEDE resources under Award PHY-130045 (D.J.M., C.C., N.W.B.). This work was supported by the U.S. National Science Foundation's CAREER program under Award CHE-1253143 (J.E.M., P.J.S.). This work was also supported by the U.S. Department of Energy, Basic Energy Sciences, under Award DE-SC0010536 (J.P.C., G.L.). G.L. was supported by a Notre Dame Energy postdoctoral fellowship.

■ REFERENCES

(1) Stockman, M. I. *Opt. Express* **2011**, *19*, 22029−22106.

(2) Nie, S.; Emory, S. R. *Science* **1997**, *275*, 1102−1106.

(3) Zhang, Y.; Zhen, Y.-R.; Neumann, O.; Day, J. K.; Nordlander, P.; Halas, N. J. *Nat. Commun.* **2014**, *5*, 4424.

(4) Morton, J.; Day, E.; Halas, N.; West, J. Nanoshells for Photothermal Cancer Therapy. In *Cancer Nanotechnology*; Grobmyer, S. R., Moudgil, B. M., Eds.; Humana Press: New York, 2010; Vol. *624*, pp 101−117.

(5) Atwater, H. A.; Polman, A. *Nat. Mater.* **2010**, *9*, 205−213.

(6) Aydin, K.; Ferry, V. E.; Briggs, R. M.; Atwater, H. A. *Nat. Commun.* **2011**, *2*, 517.

(7) Tian, Y.; Tatsuma, T. *Chem. Commun.* **2004**, 1810−1811.

(8) Liu, Z.; Hou, W.; Pavaskar, P.; Aykol, M.; Cronin, S. B. *Nano Lett.* **2011**, *11*, 1111−1116.

(9) Chen, H. M.; Chen, C. K.; Chen, C.-J.; Cheng, L.-C.; Wu, P. C.; Cheng, B. H.; Ho, Y. Z.; Tseng, M. L.; Hsu, Y.-Y.; Chan, T.-S.; Lee, J.-F.; Liu, R.-S.; Tsai, D. P. *ACS Nano* **2012**, *6*, 7362−7372.

(10) Schaadt, D. M.; Feng, B.; Yu, E. T. *Appl. Phys. Lett.* **2005**, *86*, 063106.

(11) Sachan, R.; Gonzalez, C.; Dyck, O.; Wu, Y.; Garcia, H.; Pennycook, S. J.; Rack, P. D.; Duscher, G.; Kalyanaraman, R. *Nanomater. Energy* **2013**, *2*, 11−19.

(12) Nakayama, K.; Tanabe, K.; Atwater, H. A. *Appl. Phys. Lett.* **2008**, 93, 121904.

(13) Li, J.; Cushing, S. K.; Bright, J.; Meng, F.; Senty, T. R.; Zheng, P.; Bristow, A. D.; Wu, N. *ACS Catal.* **2012**, 3, 47−51.

(14) Cushing, S. K.; Wu, N. *Interface* **2013**, *22*, 63−67.

(15) Li, J.; Cushing, S. K.; Zheng, P.; Meng, F.; Chu, D.; Wu, N. *Nat. Commun.* **2013**, *4*, 2651.

(16) Cushing, S. K.; Li, J.; Meng, F.; Senty, T. R.; Suri, S.; Zhi, M.; Li, M.; Bristow, A. D.; Wu, N. *J. Am. Chem. Soc.* **2012**, *134*, 15033−15041.

(17) DeSario, P. A.; Pietron, J. J.; DeVantier, D. E.; Brintlinger, T. H.; Stroud, R. M.; Rolison, D. R. *Nanoscale* **2013**, *5*, 8073−8083.

(18) Mukherjee, S.; Zhou, L.; Goodman, A. M.; Large, N.; Ayala-Orozco, C.; Zhang, Y.; Nordlander, P.; Halas, N. J. *J. Am. Chem. Soc.* **2014**, *136*, 64−67.

(19) Linic, S.; Christopher, P.; Xin, H.; Marimuthu, A. *Acc. Chem. Res.* **2013**, *46*, 1890−1899.

(20) Mubeen, S.; Lee, J.; Liu, D.; Stucky, G. D.; Moskovits, M. *Nano Lett.* **2015**, *15*, 2132−2136.

(21) DuChene, J. S.; Sweeny, B. C.; Johnston-Peck, A. C.; Su, D.; Stach, E. A.; Wei, W. D. *Angew. Chem., Int. Ed.* **2014**, *53*, 7887−7891.

(22) Hoggard, A.; Wang, L.-Y.; Ma, L.; Fang, Y.; You, G.; Olson, J.; Liu, Z.; Chang, W.-S.; Ajayan, P. M.; Link, S. *ACS Nano* **2013**, *7*, 11209−11217.

(23) Clavero, C. *Nat. Photonics* **2014**, *8*, 95−103.

(24) Furube, A.; Du, L.; Hara, K.; Katoh, R.; Tachiya, M. *J. Am. Chem. Soc.* **2007**, *129*, 14852−14853.

(25) Brongersma, M. L.; Halas, N. J.; Nordlander, P. *Nat. Nanotechnol.* **2015**, *10*, 25−34.

(26) Linic, S.; Christopher, P.; Ingram, D. B. *Nat. Mater.* **2011**, *10*, 911−921.

(27) Manjavacas, A.; Liu, J. G.; Kulkarni, V.; Nordlander, P. *ACS Nano* **2014**, *8*, 7630−7638.

(28) Kraus, W. A.; Schatz, G. C. *J. Chem. Phys.* **1983**, *79*, 6130−6139.

(29) Mahmoud, M. A.; Chamanzar, M.; Adibi, A.; El-Sayed, M. A. *J. Am. Chem. Soc.* **2012**, *134*, 6434−6442.

(30) Mazzucco, S.; Geuquet, N.; Ye, J.; Stéphan, O.; Van Roy, W.; Van Dorpe, P.; Henrard, L.; Kociak, M. *Nano Lett.* **2012**, *12*, 1288−1294.

(31) Ringe, E.; McMahon, J. M.; Sohn, K.; Cobley, C.; Xia, Y.; Huang, J.; Schatz, G. C.; Marks, L. D.; Van Duyne, R. P. *J. Phys. Chem. C* **2010**, *114*, 12511−12516.

(32) Sherry, L. J.; Chang, S.-H.; Schatz, G. C.; Van Duyne, R. P.; Wiley, B. J.; Xia, Y. *Nano Lett.* **2005**, *5*, 2034−2038.

(33) Nicoletti, O.; de la Pena, F.; Leary, R. K.; Holland, D. J.; Ducati, C.; Midgley, P. A. *Nature* **2013**, *502*, 80−84.

(34) Zhang, S.; Bao, K.; Halas, N. J.; Xu, H.; Nordlander, P. *Nano Lett.* **2011**, *11*, 1657−1663.

(35) Iberi, V.; Bigelow, N. W.; Mirsaleh-Kohan, N.; Griffin, S.; Simmons, P. D.; Guiton, B. S.; Masiello, D. J.; Camden, J. P. *J. Phys. Chem. C* **2014**, *118*, 10254−10262.

(36) Talebi, N.; Sigle, W.; Vogelgesang, R.; Koch, C. T.; Fernández-López, C.; Liz-Marzán, L. M.; Ögüt, B.; Rohm, M.; van Aken, P. A. *Langmuir* **2012**, *28*, 8867−8873.

(37) Luk'yanchuk, B.; Zheludev, N. I.; Maier, S. A.; Halas, N. J.; Nordlander, P.; Giessen, H.; Chong, C. T. *Nat. Mater.* **2010**, *9*, 707−715.

(38) Sonnefraud, Y.; Verellen, N.; Sobhani, H.; Vandenbosch, G. A. E.; Moshchalkov, V. V.; Van Dorpe, P.; Nordlander, P.; Maier, S. A. *ACS Nano* **2010**, *4*, 1664−1670.

(39) Ye, J.; Wen, F.; Sobhani, H.; Lassiter, J. B.; Dorpe, P. V.; Nordlander, P.; Halas, N. J. *Nano Lett.* **2012**, *12*, 1660−1667.

(40) Gallinet, B.; Martin, O. J. F. *ACS Nano* **2013**, *7*, 6978−6987.

(41) Verellen, N.; Sonnefraud, Y.; Sobhani, H.; Hao, F.; Moshchalkov, V. V.; Dorpe, P. V.; Nordlander, P.; Maier, S. A. *Nano Lett.* **2009**, *9*, 1663−1667.

(42) Fan, J. A.; Wu, C.; Bao, K.; Bao, J.; Bardhan, R.; Halas, N. J.; Manoharan, V. N.; Nordlander, P.; Shvets, G.; Capasso, F. *Science* **2010**, *328*, 1135−1138.

(43) Li, G.; Abbott, J. K. C.; Brasfield, J. D.; Liu, P.; Dale, A.; Duscher, G.; Rack, P. D.; Feigerle, C. S. *Appl. Surf. Sci.* **2015**, *327*, 7−12.

(44) Chance, R. R.; Prock, A.; Silbey, R. Molecular Fluorescence and Energy Transfer Near Interfaces. In *Advances in Chemical Physics*; John Wiley & Sons, Inc.: Hoboken, NJ, 1978; pp 1−65.

(45) Nordlander, P.; Oubre, C.; Prodan, E.; Li, K.; Stockman, M. I. *Nano Lett.* **2004**, *4*, 899−903.

(46) Bigelow, N. W.; Vaschillo, A.; Iberi, V.; Camden, J. P.; Masiello, D. J. *ACS Nano* **2012**, *6*, 7497−7504.

(47) Bigelow, N. W.; Vaschillo, A.; Camden, J. P.; Masiello, D. J. *ACS Nano* **2013**, *7*, 4511−4519.

(48) Liu, G. L.; Long, Y.-T.; Choi, Y.; Kang, T.; Lee, L. P. *Nat. Methods* **2007**, *4*, 1015−1017.

(49) Kumashiro, Y. *Electric Refractory Materials*; Marcel Dekker Inc.: New York, 2000; pp 557−585.

(50) Goossens, A.; Kelder, E. M.; Schoonman, J. *Ber. Bunsen-Ges.* **1989**, *93*, 1109−1114.

(51) Robertson, J. *J. Vac. Sci. Technol., B* **2000**, *18*, 1785−1791.

(52) Vishkasougheh, M. H.; Tunaboylu, B. *Energy Convers. Manage.* **2013**, *72*, 141−146.

(53) Himpsel, F. J.; McFeely, F. R.; Taleb-Ibrahimi, A.; Yarmoff, J. A.; Hollinger, G. *Phys. Rev. B* **1988**, *38*, 6084−6096.

(54) Mott, N. F. *Adv. Phys.* **1977**, *26*, 363−391.

(55) Schroten, E.; Goossens, A.; Schoonman, J. *J. Appl. Phys.* **1998**, *83*, 1660−1663.

(56) Wettling, W.; Windscheif, J. *Solid State Commun.* **1984**, *50*, 33−34.

(57) Malitson, I. H. *J. Opt. Soc. Am.* **1965**, *55*, 1205−1208.

(58) Pierce, D. T.; Spicer, W. E. *Phys. Rev. B* **1972**, *5*, 3017−3029.

(59) Sarney, W. L. U.S. Army Research Laboratory, Adelphi, MD, 2004; ARL-TR-3223.

(60) Johnson, P. B.; Christy, R. W. *Phys. Rev. B* **1972**, *6*, 4370−4379.

(61) Sundararaman, R.; Narang, P.; Jermyn, A. S.; Goddard Iii, W. A.; Atwater, H. A. *Nat. Commun.* **2014**, *5*, 5788.